metals

MDPI

Article

Effect of Mo Element on the Mechanical Properties and Tribological Responses of CoCrFeNiMo*x* High-Entropy Alloys

Ying Liu [1,†], Yongxin Xie [1,†], Shaogang Cui [1,2,*], Yanliang Yi [1,2,*], Xuewei Xing [1], Xiaojian Wang [1] and Wei Li [1]

[1] Institute of Advanced Wear & Corrosion Resistant and Functional Materials, Jinan University, Guangzhou 510632, China; liuying2000@jnu.edu.cn (Y.L.); xieyongxin@stu2018.jnu.edu.cn (Y.X.); xxwhym1228@stu2019.jnu.edu.cn (X.X.); xiaojian.wang@jnu.edu.cn (X.W.); Lwxasn@sohu.com (W.L.)

[2] Shaoguan Research Institute of Jinan University, 168 Muxi Avenue, Shaoguan 512027, China

* Correspondence: sgcui@jnu.edu.cn (S.C.); ylyi192@jnu.edu.cn (Y.Y.); Tel.: +86-13802425607 (S.C.); +86-15091339192 (Y.Y.)

† Ying Liu and Yongxin Xie contributed equally to this work.

Abstract: Certain amounts of precipitate in CoCrFeNiMo*x* (simplified as Mo*x*) is beneficial to the wear resistance; however, the optimal chemical content of Mo and the anti-wear mechanism behind it remains unclear. The Mo*x* (x = 0, 0.3, 0.5, 1, 1.5 in molar ratio) high entropy alloys (HEAs) were manufactured, the evolution of their microstructure, mechanical, friction, and wear properties with Mo content was studied. The results displayed that the mechanical properties of the FCC solid solution were enhanced from Mo0 to Mo0.3, then kept unchanged till x = 1.5. The volume fraction of the precipitates increased with Mo content. The Mo1 presents the lower average friction coefficient and wear rate, attributed to the desired types, amount, size, distribution of the hard σ and μ phases in the ductile FCC solid solution. The detailed mechanism behind their tribological behaviors were discussed in the manuscript.

Keywords: high-entropy alloy; microstructure; mechanical properties; CoCrFeNiMo*x*; friction and wear

check for updates

Citation: Liu, Y.; Xie, Y.; Cui, S.; Yi, Y.; Xing, X.; Wang, X.; Li, W. Effect of Mo Element on the Mechanical Properties and Tribological Responses of CoCrFeNiMo*x* High-Entropy Alloys. *Metals* **2021**, *11*, 486. https://doi.org/10.3390/met11030486

Academic Editor: Jiro Kitagawa

Received: 13 February 2021
Accepted: 5 March 2021
Published: 15 March 2021

Publisher's Note: MDPI stays neutral with regard to jurisdictional claims in published maps and institutional affiliations.

Copyright: © 2021 by the authors. Licensee MDPI, Basel, Switzerland. This article is an open access article distributed under the terms and conditions of the Creative Commons Attribution (CC BY) license (https://creativecommons.org/licenses/by/4.0/).

1. Introduction

High entropy alloys (HEAs), namely the multicomponent alloys, have become a hotspot of material research since 2004 when proposed by Yeh et al. [1] and Cantor et al. [2]. Because they possess high thermal stability, superior physical and excellent mechanical properties, such as high hardness [3], high strength, and high ductility, especially at a cryogenic temperature [4,5], excellent wear resistance [6], and corrosion resistance [7], which make the HEAs the promising materials as components in structural and mechanical materials, particularly at cryogenic temperature. These special features have been on account of the high mixing entropy, sluggish diffusion, and severe lattice distortion. HEAs are composed of five or more principal elements with the concentration of each element being between 5 wt.% and 35 wt.%, they have a stable solid-solution state attributed to the high mixing entropy $\Delta Smix$, and the distribution of the five constituent elements is relatively random and uniform [8].

HEAs such as CoCrFeNi alloy systems, with a face-centered (FCC) structure, have attracted many attentions due to their exceptional ductility, fracture toughness, and high work hardening capability [9]. Gludovatz et al. had researched the mechanical properties of CrMnFeCoNi HEA, the results show that it has better toughness and yield strength than most pure metals and alloys, and has the comparable strength as structural ceramics, closing to the strength of some bulk metallic glasses [10]. However, the HEA matrix alone, especially the single-phase catalytic cracking structure, is not enough for engineering applications at room temperature. For example, the single-faced CoCrFeNi HEA with an FCC structure has a yield strength of only 155 MPa and a tensile strength of 472 MPa [11].

As a result, Mo element is usually added to the single-phase CoCrFeNi FCC solid solution. to obtain a combination of high strength and excellent ductility, for pursuit solid solution strengthening and precipitation hardening. This is because the Mo atom has a large atomic size for both solid solutions caused by the higher lattice distortion and precipitation hardening [12,13]. Mo can promote the precipitation of hard and brittle (Cr,Mo)-rich σ and (Mo,Cr)-rich μ phases in a FCC solid solution. It will increase the strength and hardness but reduce the ductility [14]. When the molar ratio of Mo is beyond 0.3, it shows the emergence of a dendritic structure and forms hard intermetallic phases with Co, Cr, Fe, and Ni elements [15]. Liu et al. [11] had used a thermal calculation computer program to evaluate the phase stability of a complex multi-component system and calculated the (CoCrFeNi)-Mo pseudo-binary phase diagram. It suggests that with the increasing Mo element the microstructures of the as-cast Mo0.2 and Mo0.3 alloys develop to a dendritic microstructure, and Mo starts to segregate in the inter-dendritic areas in the as-cast Mo0.3 alloy showing a mixed two-phase structure (FCC + σ). When the molar ratio is beyond 0.3, then three phases (FCC+ σ + μ) form. The precipitation of these hard topologically close-packed (TCP) phases (σ and μ) with a highly high hardness of 15 GPa has a substantial influence on the mechanical properties of FeCoCrNi based high entropy alloys, which strongly affect their tribological behavior as well [11,14]. Li et al. had studied the fracture performance and fracture mechanism of CoCrFeNiMo0.2 high entropy alloy, revealing that the alloy possesses a good damage tolerance at room temperature [16]. Besides, the study of fracture mechanism shows that the boundary between the grain and intermetallic precipitation is the weak part of the microporous nucleation, and the cracks mainly propagate along the interface between grain boundary and precipitation particles. Niu et al. [17] investigated the as-annealed FeCoCrNiMo*x* high entropy alloys, revealing annealing treatment induces Mo addition to be unstable, and the phase separation happens. Bae et al. studied cold rolling and subsequent annealing treatment at different temperature of Co17.5Cr12.5Fe55Ni8Mo5 alloys, the structure is composed of FCC and μ phase, μ phase is the Mo-rich phase [18], but the mechanical/wear properties is less probing. Deng et al. had investigated the fraction of Mo on the wear resistance of FeCoCrNiMo*x* (x = 0~0.3) HEAs made by spark plasma sintering and cold rolling [19]. It had found that the wear resistance improves continuously with the increase of Mo content in the range of x = 0~0.3. The revealing of microstructure evolution in subsurface and near surface suggested that though some partially tribo-oxidized wear debris formed the loosely agglomerated patches, the dominant FCC solid solution failed to be tribo-oxidized. The direct metal/metal contact takes place. However, this study did not further explore the Mo molar fraction beyond 0.3, in which the hard-intermetallic precipitation forms. The excellent deformation ability makes the CoCrFeNi be an ideal FCC solid solution for the strengthening of various intermetallic compounds. The homogeneous precipitation of hard intermetallic particles is a powerful method to strengthen the steel and alloys due to their resistance to gliding dislocations, and the precipitation strengthening depends on the type, size, number density, and distribution of the precipitated phase. Therefore, the tribological behaviors of Mox with Mo molar fraction beyond 0.3 shall be studied to reveal the ideal elemental composition.

Mo is the σ/μ phase accelerating element. In order to obtain the FCC + σ + μ phase structure, molybdenum is added as a variable element, trying to explore the influence of the variation of σ/μ phase on the alloy structure and properties. This paper was designed to investigate the effect of Mo element on the tribological behavior of Mo*x* HEAs, where x was in a much wider range of 0~1.5). It aims to find the optimal Mo content at which the lower average friction coefficient and wear rate were simultaneously achieved. The effect of Mo content on the microstructure, mechanical properties and friction and wear properties of the HEAs alloys were also investigated in detail, and the anti-wear mechanism behind the optimal chemical compositions was revealed.

2. Materials and Methods

The CoCrFeNiMox (x = 0, 0.3, 0.5, 1, 1.5 in atomic proportion) alloys were prepared by vacuum arc melting method melted in a water-cooled copper mold under high purity argon atmosphere. For convenience, these prepared alloys are referred to as Mo0, Mo0.3, Mo0.5, Mo1, and Mo1.5, respectively.

High purity elements (≥99.9 wt.%) were used as raw materials. The FeCoCrNiMox ingots were remelted at least five times to improve the chemical homogenous distribution. The microstructures, physical and mechanical properties of these as-cast samples were characterized to evaluate the effect of Mo content on the microstructure and properties.

The friction and wear properties of the prepared Mox HEAs were evaluated using a reciprocating tribometer (Rtec Co. Ltd., San Jose, CA, USA) with a configuration of ball-on-plate. The schematic diagram of reciprocating ball-on-disc was shown in Figure 1. Before the testing, the test surfaces of fabricated samples were ground by 200#, 600#, 1000#, 2000# SiC paper and polished with 3 μm suspension, the surfaces have a surface roughness (Sa) of 0.034 μm, respectively. Then they were ultrasonically cleaned in alcohol. The YG 6 ceramic ball with a diameter of 5 mm and chemical composition of 94%WC and 6% Co was used as the counter sliding surface. The test conditions were set as the applied load of 20 N, duration of 40 min, a sliding stroke of 10 mm, reciprocating frequency of 5 HZ, which slides a total distance of 240 m. To ensure repeatability, each test was repeated at least three times. After tribological tests, the 3D surface profiles of the wear tracks on plates were measured by the 3D profiler (Rtec Co. Ltd., San Jose, CA, USA).

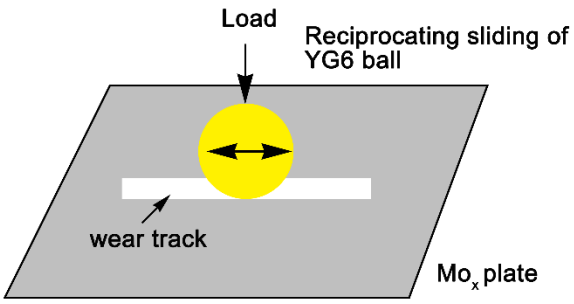


Figure 1. Schematic diagram of reciprocating ball-on-disc.

The structural features of HEAs were characterized by X-ray diffraction (XRD, UItima IV, Rigaku, Tokyo, Japan) with Kα1 radiation at 40 kV/40 mA, scanning from 30 to 60° in 2θ at a scanning speed of 5°/min. The microstructure was investigated by scanning electron microscope (SEM, Phenom XL, The Netherlands) operated at 15 kV with an energy dispersive spectrometer (EDS), and the Image Pro Plus software was used to measure the fraction of the precipitate phases.

The hardness was measured on the polished specimens with a microhardness tester (HXD-1000TMSC/LCD, Shanghai, China) at a load of 1.961 N and dwell time of 15 s. To assure accuracy, each alloy was measured with at least 5 points for averaging.

The nanoindentation hardness tests were performed on the Nanoindenter (Nano Indenter G200, Keysight Inc., Santa Rosa, CA, USA) with a Berkovich indenter at room temperature, with a loading time of 15 s, hold time of 2 s, Poisson's ratio of 0.28. The allowable drift rate was set to 0.1 nm/s, and the surface approach velocity to 10 nm/s. NanoSuite software (version 6.2, Santa Rosa, CA, USA) was used to set these parameters and collect the results. The peak load of 10 mN is used to measure the hardness of the different phases in the Mox HEA. An array of 10 × 10 indentation points was carried out for each sample. Then SEM was used to image these points, from which qualified points were selected.

The compression tests were performed using a cylinder specimen with the size of Ø 5 mm × 10 mm on an MTS E45.305 electronic universal material testing machine (MTS, Shanghai, China) at a compression rate of 1 mm/min at room temperature. The surface of

the test samples was polished down to a 2000-grit SiC paper to eliminate scratches. Each compression test was repeated three times to ensure repeatability.

3. Results

3.1. Microstructure

Figure 2 is the XRD patterns of the as-cast Mo*x* HEAs. It can be seen that all samples have a basic FCC solid solution structure. It can be seen that at $x = 0$, the FeCoCrNi alloy have a single FCC structure. Some XRD peaks belong to the σ phase appears when $x \geq 0.3$. When $x \geq 1$, Mo*x* alloys exhibits an FCC + σ + μ multiphase structure. Figure 3 presents the corresponding SEM backscattering micrographs of the microstructure of these Mo*x* HEAs and the variation of volume fraction of the precipitates with the Mo molar ratio was given in Figure 3f. Table 1 presents the chemical compositions of the different phases in Mo*x* measured by EDS, it revealed that a significant amount of Mo and Cr was in σ phase due to their high molar ratio, especially for Mo1 and Mo1.5, the Mo: Fe molar ratio reaches 1.64 and 2.28, respectively, and even higher molar ratio was in the bright μ phase. Figure 4 presents the EDS results of the different phases (labeled as "*") in Mo*x*. For Mo0, because the Fe (1.27 Å), Co (1.25 Å), Cr (1.27 Å), and Ni (1.24 Å) atoms have similar atomic sizes, and there is no significant negative or positive atom pair mixing enthalpy between each element atoms [20], therefore, it has a single FCC solid solution structure. The bulky grains have an average diameter of 53 ± 15 μm. When the Mo molar ratio grows to 0.3, the diffraction peak beside the FCC (111) was detected, in combination with the SEM image in Figure 3b EDS analysis in Figure 4, this peak is belonging to the σ phase. Table 2 displayed the crystallite sizes and lattice parameters of σ/μ phases. The σ phase is indexed as the tetragonal structure (a = 9.2443 Å, c = 4.7921 Å, c/a = 0.5183) and the σ phase is indexed as the hexagonal structure (a = 3.5778 Å, c = 25.7538 Å, c/a = 7.1982). Further detailed analysis in Figure 3b reveals that the fraction of the precipitates was estimated to be about 3.2%. Such σ phase is usually hard and brittle, the existence of σ phase will deteriorate the inter-grain embrittlement, which is normally deleterious to the mechanical properties [21], but it could be beneficial to the abrasion resistance to some extent due to the superior hardness [11]. When the Mo molar ratio continues to be increased, the secondary phase precipitates more evidently in the Mo0.5 alloy, which includes the σ and μ phases, as indicated in the inset of Figure 3c. The total volume fraction of the secondary phases was estimated to be 14.8%, including the 12.1% σ and 2.7% μ phases. It was also noted that the μ phase was formed on the fringes of the σ phase, which was reported that it was formed through the transformation the σ phase during the solidification [14]. Figure 4 reveals that the μ phase is rich in Mo and some Cr, and the σ phase in Cr and some Mo element. It is obvious that the size and number of the secondary phase increase significantly for Mo1 and Mo1.5, displaying more dendritic structure, 48% secondary phases including 25% σ and 23% μ was estimated for Mo1. With the Mo molar ratio being increased to 1.5, and the secondary phase turns out to be μ phase dominantly with the diameter between 29–81 μm and the fraction of the secondary phase is estimated to be 77.5%. Mo1.5 alloy exhibits more μ phase and less σ phase compared with Mo1 alloy, which is because the excess molybdenum content makes for converting the σ phase into μ phase [14].

The lattice distortion was also introduced by the Mo addition. As shown in Figure 2, the main diffraction peak for FCC (111) plane locates at 43.5° for $x = 0$. It deviates to 43.1° for $x = 0.3$, this is because the atomic radius of Mo (1.39 Å) is larger, compared with the other four constitutional elements, the addition of Mo into the FCC solid solution will cause pronounced lattice distortion. When the Mo molar ratio continues to increase, the diffraction peak shows little change. This indicates that the content of Mo in the FCC solid solution lattice reaches the saturation state.

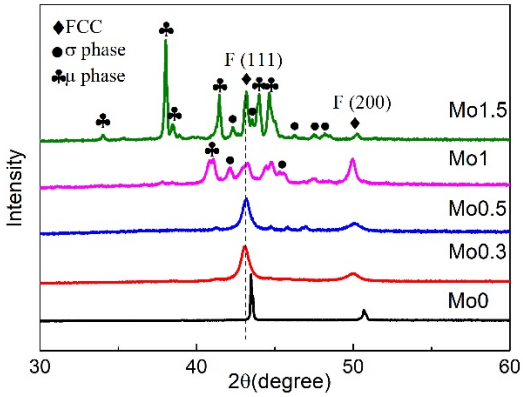


Figure 2. XRD patterns of the as-cast Mo*x* high entropy alloys.

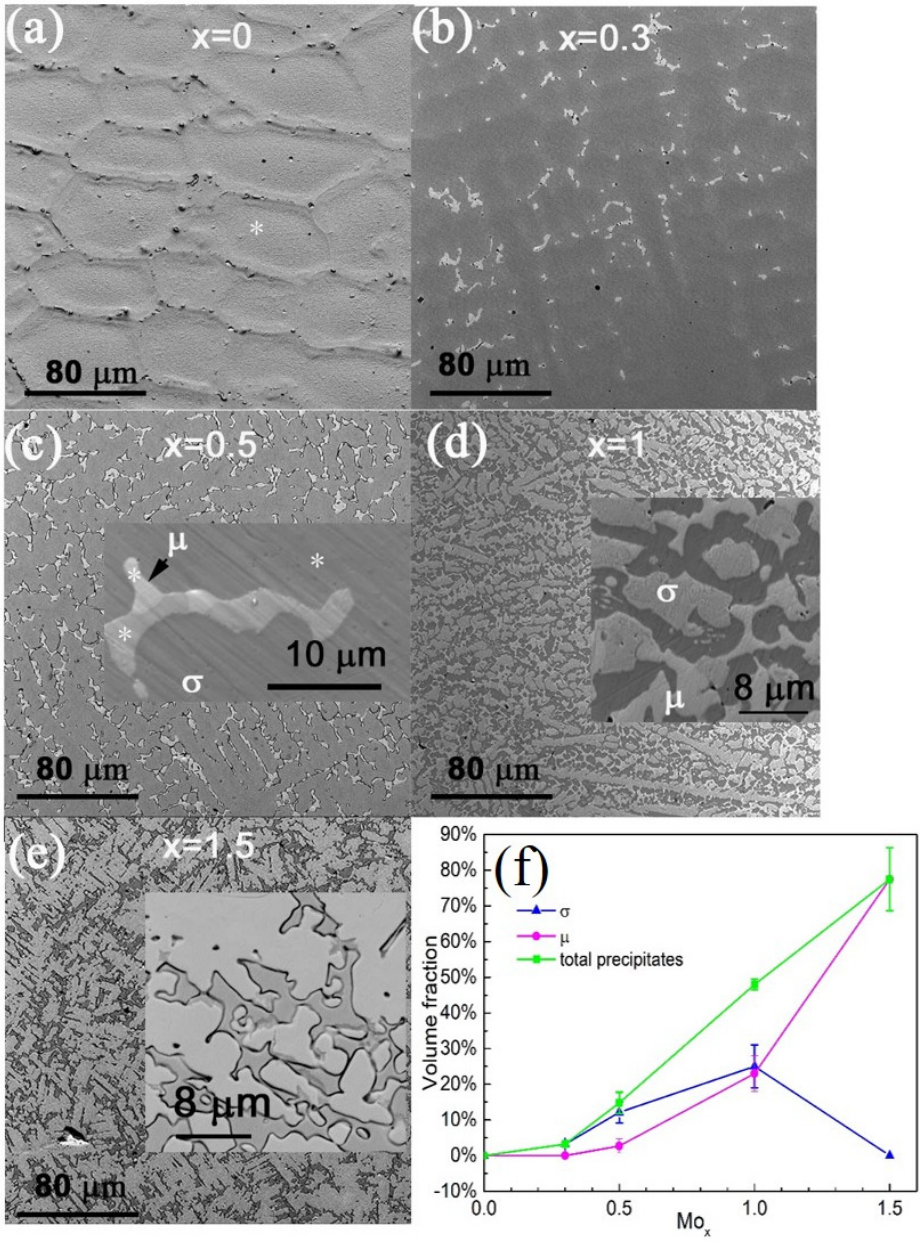


Figure 3. SEM backscattering images of the as-cast Mox high entropy alloys: (**a**) For Mo0, (**b**) for Mo0.3, (**c**) for Mo0.5, (**d**) for Mo1, (**e**) for Mo1.5, and (**f**) the variation of the volume fraction of the precipitates with the Mo molar ratio.

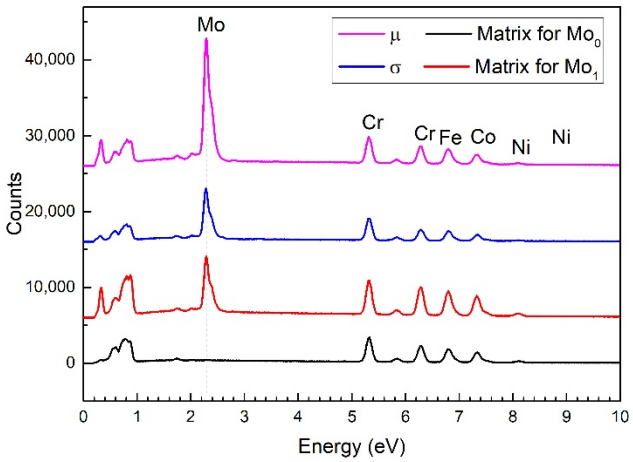


Figure 4. EDS analysis of the elements for different phases.

Table 1. Chemical composition of the different phases in the studied compounds (normalized molar ratio).

HEAs	Analyzed Area	Normalized Atomic Molar Ratio by Dividing the Fe Atoms				
		Fe	Co	Cr	Ni	Mo
Mo0	FCC solid solution	1	1.01	0.99	1.04	0
Mo0.3	FCC solid solution	1	0.99	0.88	1	0.31
	σ	1	1.08	1.49	0.83	1.42
Mo0.5	FCC solid solution	1	0.98	0.84	1.09	0.47
	σ	1	1.04	1.34	0.89	1.59
Mo1	FCC solid solution	1	1.05	0.85	1.16	0.8
	σ	1	1.07	1.16	0.93	1.64
	μ	1	1.12	1.12	0.95	1.94
Mo1.5	FCC solid solution	1	0.96	0.79	1.19	0.96
	σ	1	1.05	1.01	0.96	2.28
	μ	1	1.0	1.12	0.88	2.56

Table 2. The crystallite sizes and lattice parameters of σ/μ phases.

Phase	Lattice Parameters			Crystallite Size
σ phase	a = 9.165 Å	c = 4.739 Å	c/a = 0.517 Å	16–33 μm
μ phase	a = 4.757 Å	c = 25.589 Å	c/a = 5.379 Å	29–81 μm

3.2. Nanoindentation Results

Figure 5a presents the load-depth curves of the different phases in the HEA and SEM images of these indents, please note that these indents were only some examples. The calculated results were listed in Table 3. Firstly, 10 × 10 indents were conducted, then they were imaged by SEM, from which qualified indents were selected. For example, representative indents for σ, μ, and FCC solid solution were shown in Figure 5b. For the FCC solid solution, it can be found that the Mo0.3–1.5 HEA has a similar load-depth curve, indicating similar mechanical properties. Mo0 has a different load-depth curve, which shows a larger depth than Mo0.3–1.5. This represents the Mo0 FCC solid solution has a weak penetration resistance.

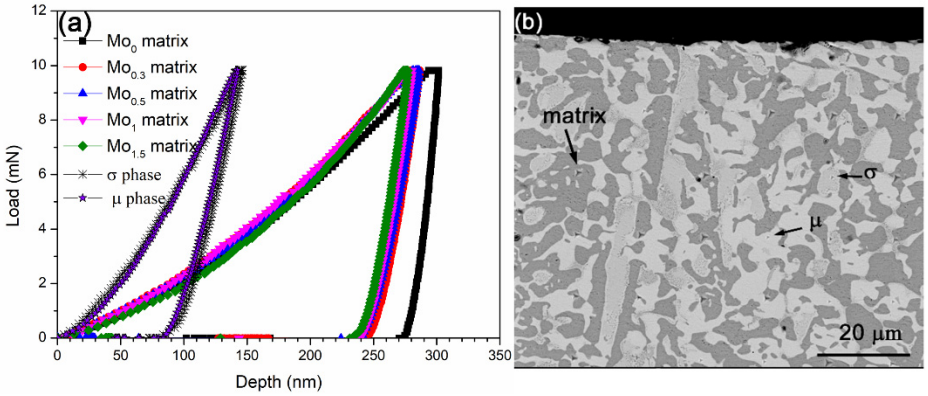


Figure 5. (**a**) Load-depth curves for the FCC solid solution, σ and μ phases in the Mo*x* HEA for the maximum load of 10 mN and (**b**) a given SEM backscattering image of these indents for Mo1.

Table 3. The nano-hardness of the prepared materials in different phases.

Materials	Hardness (GPa)
YG6 ball	20 ± 0.5
Mo0 FCC solid solution	3.8 ± 0.1
FCC solid solution for Mo0.3, Mo0.5, and Mo1.5	4.7 ± 0.2
σ phase	21 ± 1.2
μ phase	21 ± 1.7

Table 3 shows the nanohardness of the prepared Mo*x* HEAs measured by nanoindenter. A heavy load of 300 mN was applied to measure the global mechanical response of YG 6. It found that the counter YG6 ball has a hardness of 20 ± 0.5 GPa. Then a light load of 10 mN was used to measure the mechanical response of the separate phases in the Mox HEA. From Figure 5 and Table 3, it can be found that the μ has a similar hardness to that of the σ phase. They were also similar to that of YG 6 ball in hardness. The Mo-saturated FCC solid solution for Mo0.3–1.5 has a hardness 0.9 GPa higher than that of Mo0 FCC solid solution. The nanoindentation results prove that the mechanical strength of the matrix strengthened by solid solution reaches the maximum when the molar ratio of Mo increases to 0.3. Further increase in Mo molar ratio contributes little to the increase of mechanical strength of the matrix, but it will increase volume fraction of the precipitated intermetallic. This becomes the dominant factor in determining mechanical properties.

3.3. Mechanical Properties of Fabricated Mox

Figure 6a presents the compressive engineering stress–strain relationship and the microhardness of the HEAs. A high load of 1.961 N was adopted to measure the microhardness, therefore, it reflects the global mechanical response of the Mo*x* HEA. The Mo0 presents low compressive yield stress of 207 MPa and hardness of 161.4 HV but shows excellent ductility. When the Mo molar ratio increases to 0.5, with the intermetallic precipitated increasingly, the yield stress and hardness increase steadily, and the ductility does not show pronounced deterioration. When the Mo molar ratio increases to 1, the yield stress and hardness increase to 825 MPa and 550.2 HV, respectively, but the ductility also shows an obvious decline. The fracture stress is 1822.4 MPa, in a strain of 11.4%. The Mo1.5 presents an obvious brittle fracture nature with the fracture stress of 996 MPa and hardness of 779 HV, not presenting any plastic deformation behavior. Such superior hardness and inferior ductility might be due to the overly high fraction volume of the precipitated intermetallic, as shown in Figure 3e,f.

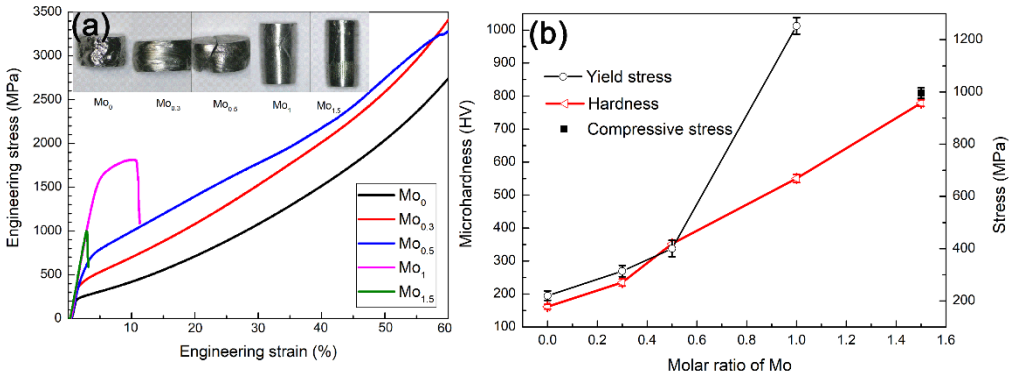


Figure 6. (**a**) Compressive engineering stress-strain curves of Mo*x* high entropy alloys, in which the photos of the cylindrical samples of Mo*x* HEAs after compression tests were inset, and (**b**) Vickers hardness, yield and compressive stress obtained from (**a**).

Figure 7 presents the SEM images of the fractured surface after compressive tests. For Mo1, cracks in the particles are observed, indicating an inter-particle fracture. The FCC solid solution presents a ductile fracture, surrounding the particles. The brittle fracture in the particles becomes more evident for Mo1.5, presenting very little ductile deformation. The crack mainly initiated along grain boundary/precipitate interfaces and large intermetallic particles.

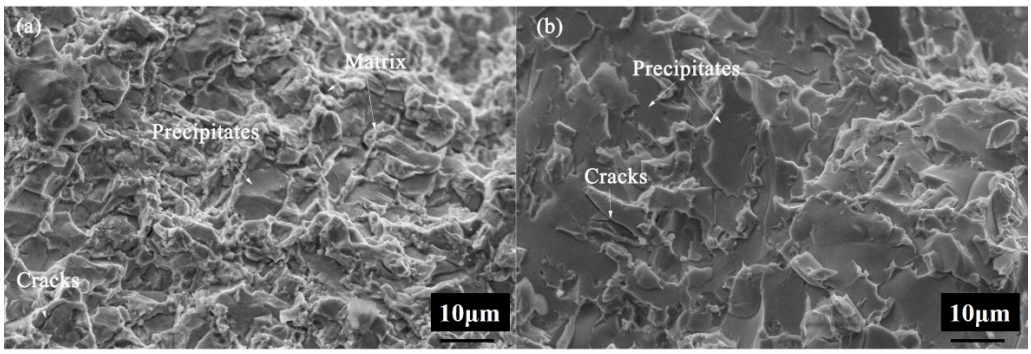


Figure 7. SEM secondary electron images of the fractured surface for (**a**) Mo1 and (**b**) Mo1.5 after compressive tests.

3.4. Tribological Behavior

Figure 8a shows the variation of friction coefficient with sliding distance for the Mo*x* HEAs, and Figure 8b shows the average friction coefficient. It can be observed that the Mo0 and Mo0.3 generate the highest friction coefficient at approximately 0.62, when sliding against YG6 ball, followed by Mo1.5 at 0.45 and Mo0.5 at 0.39, the Mo1 shows the lower friction coefficient at 0.35. The FeCoCrNi alloy is soft and during the wear process, the more debris accumulated on the worn surface maybe increase the roughness of the worn surface and increased the friction coefficient. The increase of the Mo additive increased the hard secondary phase content and reduced the friction coefficients, it can be inferred that the reciprocating wear resistance can be improved. From Figure 8b we can see Mo1 alloy shows the lower average friction coefficient.

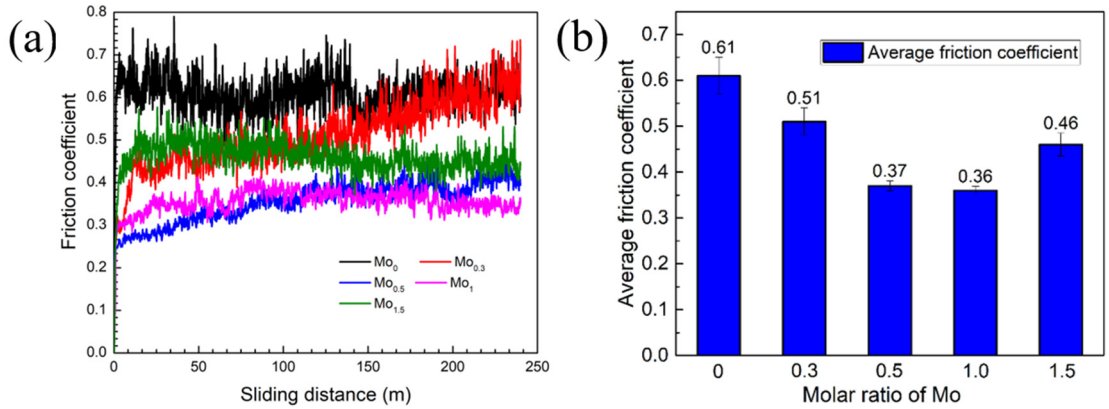


Figure 8. (**a**) Evolution of friction coefficients with the sliding distance for the Mo*x* HEAs in wear process after 240 m sliding under 20 N at a speed of 0.1 m/s, (**b**) the average friction coefficient of Mo*x* alloys.

3.5. Surface Profilometry

Figure 9a,b exhibit the 3D profilometry of the wear tracks after 240 m sliding wear test under the load of 20 N at 0.1 m/s. The color change in the figure means the wear track depth change as illustrated in Figure 9b. Mo0 alloy has a maximum depth of 209 μm and a maximum width of 2140 μm. With the increase of Mo molar ratio, both the depth and width of the wear track decreased till the molar ratio of Mo reaches 1.5, whose wear track grows wider and deeper than that of Mo1. This indicates that Mo1 alloy has the lowest depth and width among the tested HEAs, which shows the best wear resistance.

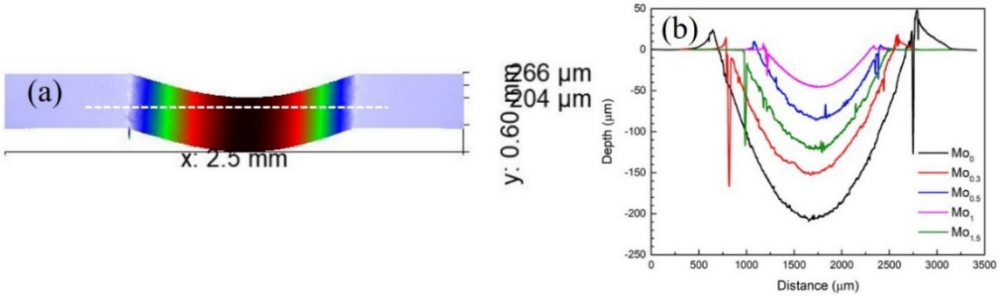


Figure 9. (**a**) Representative 3D profilometry of the wear tracks for Mo1 and (**b**) the measured wear track profiles for the wear tracks of samples with different Mo molar ratios.

Figure 10 shows the variation of volume wear loss, wear rate, and average surface roughness (Sa) with the molar ratio of Mo. The volume loss is obtained by multiplying the cross-sectional area of the wear track by the length of the wear track, the values of which is averaged from at least three wear tests. The wear rate in this paper is calculated according to Archard's law: $K = V/(F \times L)$ [22]. The parameters of K, V, F, and L indicate the wear rate, wear volume (mm^3), applied load (N) and total sliding distance (m), respectively. The trend of the volume loss confirmed the best wear resistance of Mo1 HEA. In addition, to further enrich and accurately explore the wear resistance of the material, we also calculated the wear rate of the Mo*x* HEAs. As presented in Figure 10, the wear rate of Mo*x* HEAs shows the same trend as volume loss and Sa. The wear rate has a rapid decline in Mox alloy, the wear rate of Mo*x* alloy is about 8.5×10^{-5} $mm^3/(N \cdot m)$. When the Mo molar ratio increased up to 1, there is an obvious decreased trend in wear rate, declining to 8.25×10^{-6} $mm^3/(N \cdot m)$. In this paper, the effect of Mo concentration on the wear behavior of Mox HEAs is consistent with previous studies [13,23]. The roughness of the wear scar is consistent with the amount of wear loss and the friction coefficients in Figure 9, which shows that the stronger wear resistance of the material will result in a lower Sa, which then leads to a lower friction coefficient.

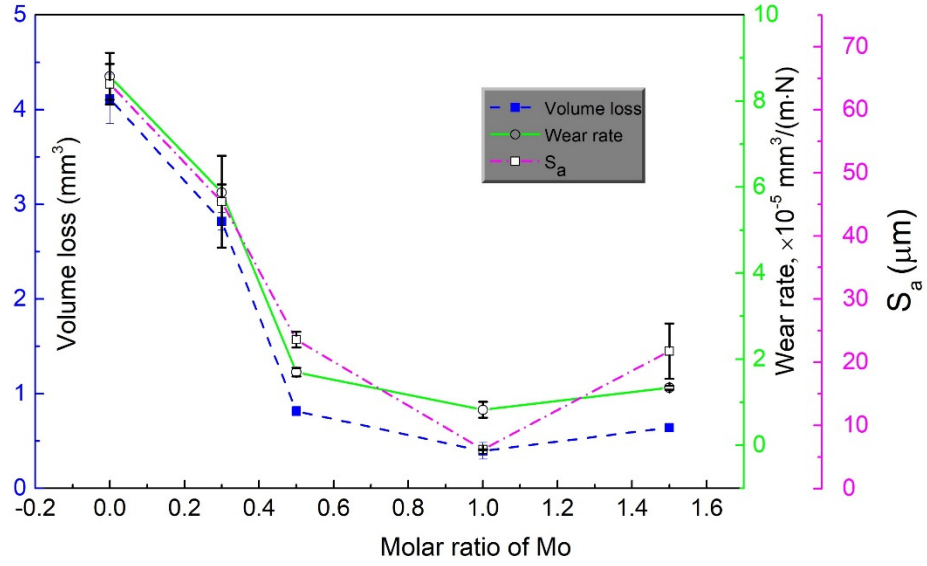


Figure 10. Volume loss, specific wear rates, and the average surface roughness (Sa) of wear scars for Mox (x = 0, 0.3, 0.5, 1, 1.5) high entropy alloys.

Figure 11 presents the SEM images of the worn surface for Mo0, Mo0.3, Mo0.5, and Mo1.5 after tribological tests, and Figure 12 shows the SEM images and EDS elemental mapping of Mo1.0. From Figure 11 combined with Figure 12, it can be clearly seen that the width of wear tracks reduces gradually with the Mo molar ratio in the range of 0 to 1, then it increases from the Mo molar ratio of 1 to 1.5 with the Mo1 showing the narrowest wear track. This trend agrees well with the one obtained from the profiles of wear tracks in Figure 9. For the Mo0 HEA, as indicated in Table 3 and Figure 6, it has a low hardness of 3.8 GPa, yield stress of 207.4 MPa and superior ductility. In comparison, the YG6 possesses a superior hardness of 20.1 GPa. Therefore, the hard YG6 asperities will severely plow and deform the soft Mo0, making the Mo0 work-hardened and becomes increasingly brittle, where the maximum shear stress will be generated at a certain depth below the surface [24]. When the accumulation of the plastic deformation at the subsurface exceeds the limit, the cracks will initiate and propagate parallel to the surface, when the crack propagation reaches the surface, it will delaminate from the wear surface [25]. For Mo0.3, the plow grooves can still be observed across the wear track, the wide grooves with the width of 9.2 μm can be seen, which indicates that it was still plowed by the hard YG6 asperities. Some compressed sheets were found to cover some areas of the wear track, indicating the excellent ductility of Mo0.3. Therefore, the Mo0.3 suffers from the dominant micro-cut wear and some adhesive wear. When the Mo molar ratio continues to increase to 0.5, the micro-cut was identified to be the main wear mechanism, some micro-fatigue was also observed with some peeling-off found. Such micro-cut was severely limited for the Mo1 HEA, which suffers from mild abrasive wear. When the molar ratio of Mo increases to 1.5, the wear track becomes wider than that of Mo1 sample and was also distributed by the voids and wear debris, as shown in Figure 11g,h. The formation of these voids is mainly attributed to the micro-fracture mechanism. The hard asperities of YG6 indent the brittle Mo1.5 causing the initiation of the cracks, which will propagate. Such fractures will detach when the cracks propagate to the surface [26].

From Figure 12, it can be seen that a lot of secondary phases were detached from the worn surface, and the FCC solid solution becomes smooth. Interfacial cracks between the FCC solid solution and precipitate are observed, it is attributed to the difference of plastic deformation of the two phases under the interfacial shear stress. Cracks in the precipitate are also found, indicating the brittle fracture of the precipitate under heavy normal stress [24]. It should be noted that the brittle fracture and grain pull-out of the precipitates do not cause the large-scale mechanical damages on the worn surface, they

were mainly limited to surface damage of around 10 μm diameter. Because the hard and brittle precipitates were surrounded by the ductile FCC solid solution, the propagation of the cracks into the FCC solid solution was prevented due to the excellent ductility of the FCC solid solution.

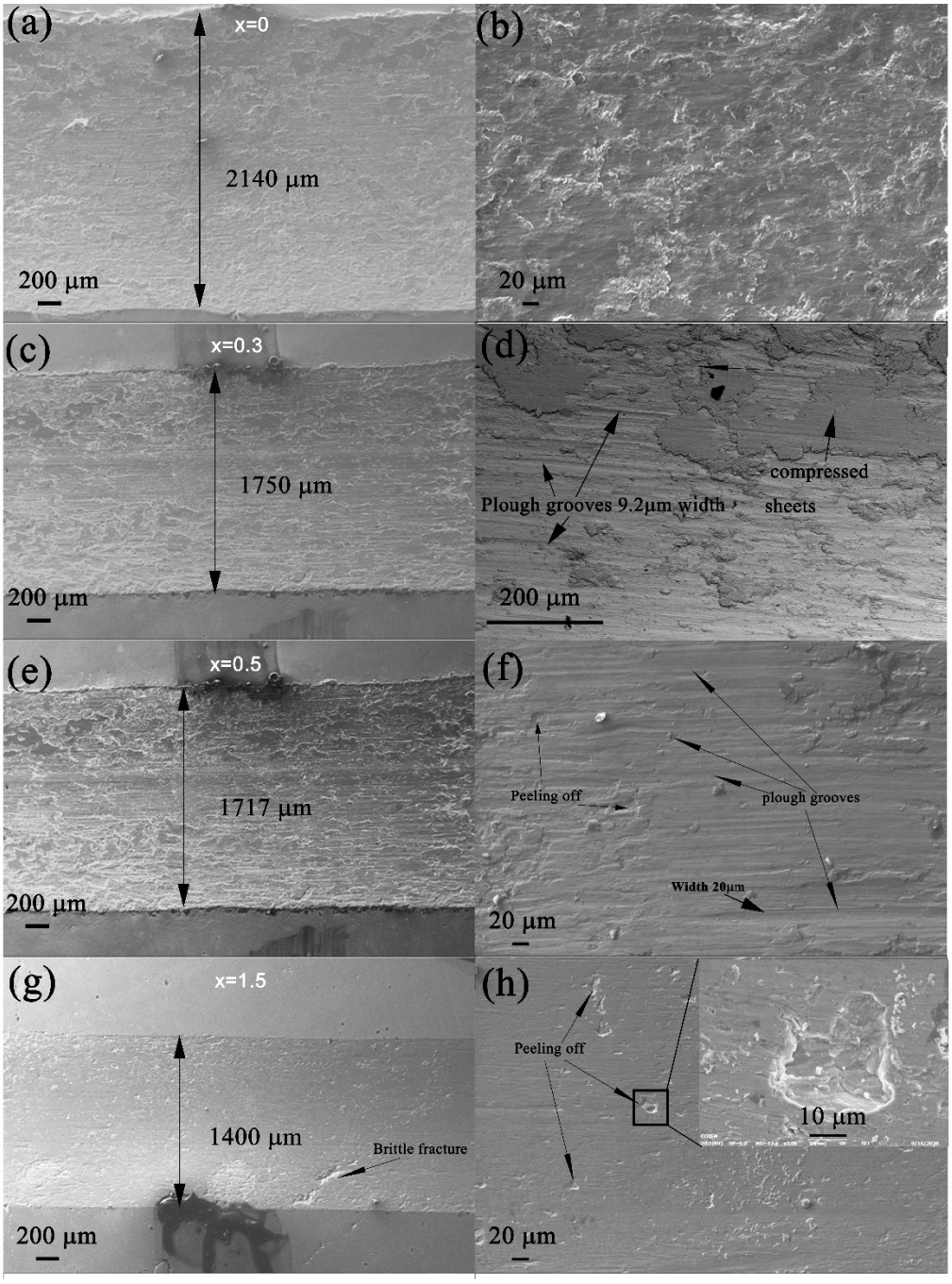


Figure 11. Volume loss, specific wear rates, and the average surface roughness (Sa) of wear scars for Mo*x* (*x* = 0, 0.3, 0.5, 1, 1.5) high entropy alloys, (**a**) and (**b**) for Mo0 alloy, (**c**) and (**d**) for Mo0.3 alloy, (**e**) and (**f**) for Mo0.5 alloy, (**g**) and (**h**) for Mo1.5.

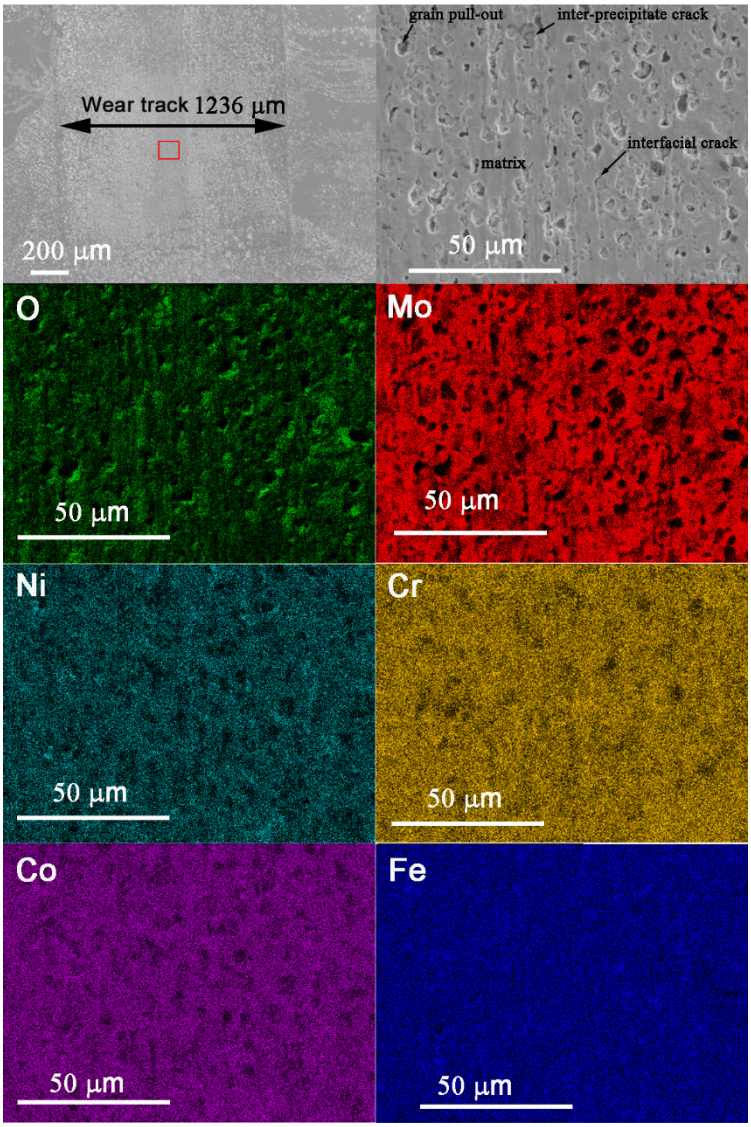


Figure 12. SEM EDS secondary electron images and elemental mapping of the wear track formed on Mo1 HEA after 240 m sliding under 20 N, the red rectangular area was further magnified to its right side.

3.6. Subsurface Characterization

Figure 13 shows the SEM images of the cross-sections of the wear tracks on HEAs, and the work-hardening behavior of the Mo0.3 and Mo0.5 FCC solid solution. As for the HEA without Mo, no obvious protective tribo-oxidation (glaze) layer on the wear track is observed, further indicating the direct YG6 /HEA contact. Such a phenomenon was mainly attributed to the strong oxidation resistance because of the massive Cr atoms. Cracks propagation from the surface to subsurface is observed, indicating an early sign of delamination wear. When the Mo molar ratio was increased to 0.3, a similar contact surface to that of Mo0 was observed, only a few precipitates with diameters less than 3 μm at the top surface are found, whose diameter is pronouncedly smaller than the width (about 9.2 μm) of the plowing grooves, as shown in Figure 11d, indicating the easy removal of these particles through micro-cutting. As for the Mo0.5, the volume fraction of the secondary phases increases slightly, which further reduces the wear rate, as shown in Figure 9. but the amount of the hard phases is still too low, only a small fraction of the top surface was occupied by the hard phase, furthermore, similar problems with the small size of these precipitates is still present, as shown in the inset of Figure 13c. This makes a lot of

the precipitates not work effectively to resist the wear. As for Mo1, the cross-sectional SEM image in Figure 13d show that a large area of the contacting surface was occupied by the precipitates, composed of both σ and μ precipitates. This indicates the majority of the load was carried by the precipitates, which have superior elastic modulus and hardness. The diameter of these precipitates is larger than those of Mo0.3 and Mo0.5, which indicates that they cannot be removed off easily. But some pull-outs of the precipitates were observed, the hard precipitation can resist the abrasion of the YG6 asperities, while the ductile FCC solid solution increases the global ductility of the HEA. For Mo1.5, the contacting surface was almost entirely covered with the hard and brittle precipitation, which indicates a major carrier of the load; however, the inter-precipitate cracks can be seen prevalently on the top surface and in the subsurface. The cracked precipitate on the top surface will be removed off easily by the shear stress, causing severe wear of Mo1.5.

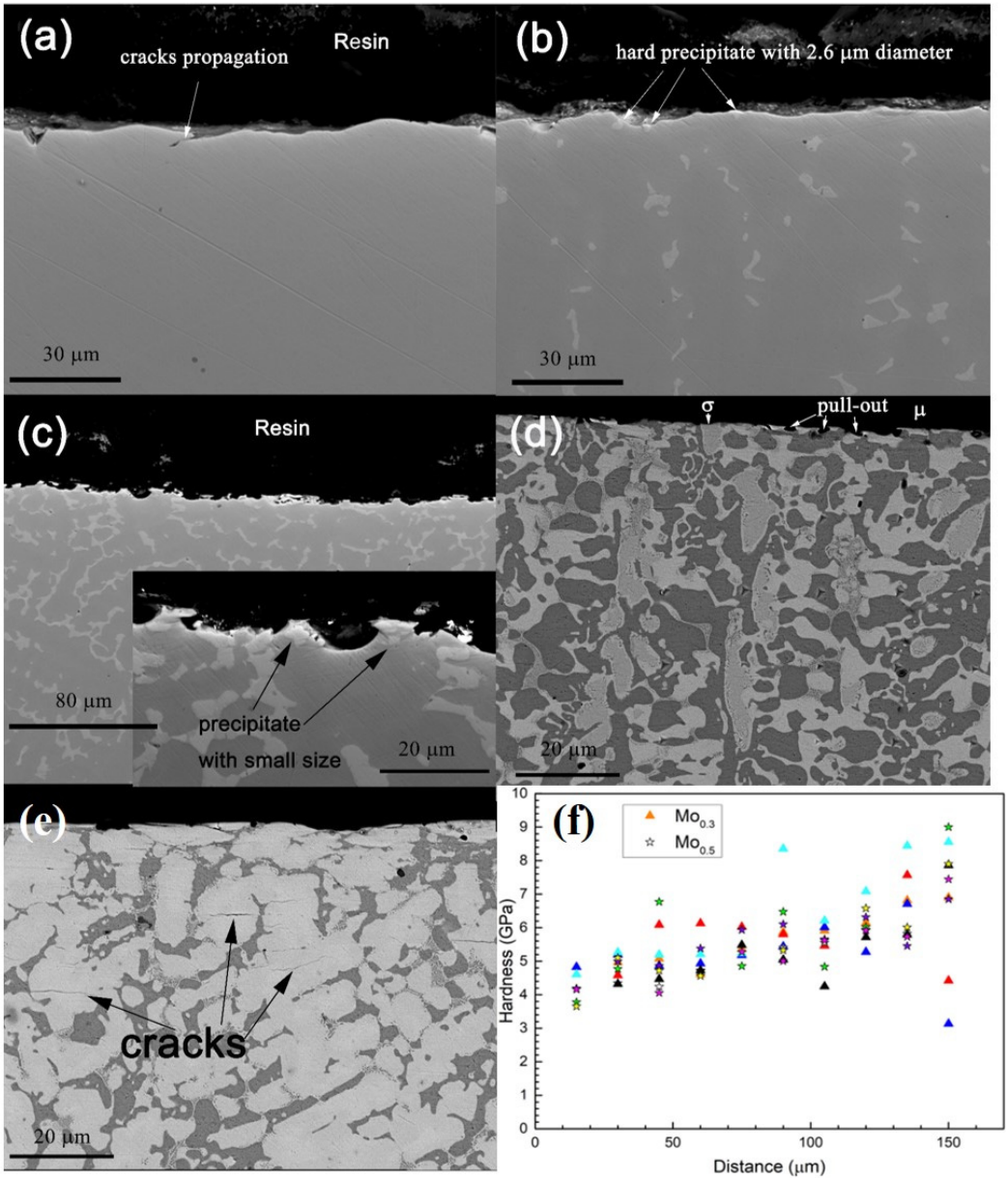


Figure 13. The SEM images of the cross-sections of the wear tracks on high entropy alloys (HEAs), and the work-hardening behavior of the Mo0.3 and Mo0.5 FCC solid solution, (**a**) for Mo0 alloy, (**b**) for Mo0.3 alloy, (**c**) for Mo0.5 alloy, (**d**) for Mo1 alloy, (**e**) for Mo1.5 alloy, (**f**) is the hardness of Mo0.3 and Mo0.5 alloy.

Figure 13f shows the hardness evolution from the top surface to the depth of the subsurface. It can be observed that obvious work hardening occurs, and the hardness of the top surface increases to 7.7 GPa from 4.7 GPa. The Mo0.3 and Mo0.5 experience similar work hardening behavior, indicating that the FCC solid solution undergoes similar plastic deformation. The detailed microstructure of the subsurface was revealed by Deng et al. [19] using FIB and STEM, it found that the subsurface can be divided into three layers: The top layer is composed of very fine nano-grains, the medium layer is the transition region, and the bottom layer belongs to the FCC solid solution. Thus, it can be concluded that the highest hardness is due to the formation of nano-grains. These nano-grains are formed due to the repeated plastic deformation of the FCC solid solution.

4. Discussion

Different from some metals, which can establish the wear-resistant glaze layer through tribo-oxidation, agglomeration, and compaction of the wear debris in the sliding process [27,28]. The tribo-oxidation of Mo*x* HEAs is believed to play a weak role in the wear resistance of Mox HEAs. From Figure 12, it can be postulated that the sliding surface of Mo*x* HEA suffers from weak oxidation. The intensity of the oxygen signal is weak except for some small areas. The cross-sectional SEM images in Figure 13 also demonstrate that no tribo-oxidation layers exist on the top sliding surfaces. This is mainly attributed to the high Cr content in the FCC solid solution and precipitates. Deng et al. analyzed the subsurface using FIB and STEM techniques, though they found that partially tribo-oxidation of wear debris occurs and loosely agglomerated; however, the dominant FCC solid solution was not oxidized [19]. Therefore, the direct sliding contact between hard YG6 and Mo*x* dominates in the entire sliding process, in which the hard precipitates play a critical role in the friction and wear responses.

The global hardness of the Mo*x* HEAs increases continuously with the Mo molar ratio, as shown in Figure 6b, which is beneficial to the improvement of abrasion resistance. The Nanoindentation results in Figure 5 suggest that the FCC solid solution is strengthened when the Mo molar ratio is increased from 0 to 0.3, further increase in Mo will not further strengthen the FCC solid solution due to the dissolution saturation of Mo. It will lead to more precipitation of the hard intermetallic. The increased volume fraction of intermetallic results in increased global hardness. Simultaneously, it will also increase the yield stress as well from Mo0 to Mo1.0. These precipitations can work as obstacles to the movement of dislocations [29], which also can reduce the plastic flow of the soft FCC solid solution. However, it will deteriorate the ductility. Therefore, when the Mo molar ratio is increased to 1.5, the HEA suffers from brittle fracture without any plastic deformation. This is mainly due to the overly high-volume fraction (77.5%) of the intermetallic precipitates, which severely break the continuity of the FCC solid solution, as shown in Figure 7. In this case, the HEA is more prone to micro-fracture when subject to external stress, and the cracks will propagate rapidly after its formation.

The Mo1 is verified to have the lower average friction coefficient and the highest wear resistance for the relative sliding process among the tested HEAs. It is because the Mo1 has the desirable combination of mechanical properties with the global hardness of 550 HV, yield stress of 825 MPa, and a compression rate of 11.4% before fracture. This is mainly attributed to the desirable size, volume fraction, and distribution of the hard-reinforcing precipitation within the ductile FCC solid solution. Many wear-resistant composites enhance their wear resistance by introducing secondary hard phases into the ductile matrix material, such as ceramic particles strengthened high chromium white cast iron composite castings used in mineral and cermet crushing industry [30], Al_2O_3 enhanced aluminum for lightweight and wear-resistant transportation material [31]. It was usually found that the wear resistance firstly improved with the increasing content of hard-secondary phases, then declined when the volume fraction of the secondary phases exceeds a certain value.

Figure 14 presents the schematic diagram of the interactive behaviors between the precipitates and YG6 asperities in the wear process under heavy normal and shear stress.

Firstly, the ductile FCC solid solution encompassing the hard phase can support the hard phase and distribute the normal and shear stress more uniformly, as shown in Figure 11 (asperity a). this could improve the load-bearing capability of the HEAs. The presence of the hard phases also can improve the global hardness to reduce the penetration of the hard asperities or abrasive particles [32], as shown in Figure 11 (asperity b). According to the friction theory suggested by Bowden and Tabor [33], the frictional resistance originated from two parts: One is the force to shear off the metallic junctions formed by adhesion and welding at the interface and the other is the plowing force to displace the softer metal from the path of the harder metal. The YG6 ceramic ball, composed of 94%WC and 6% Co, shows a dissimilar chemical nature from the Mo*x* HEAs, therefore, the role of adhesion can be negligible and the plowing force becomes the dominant factor. With a high fraction of the sliding surface occupied by hard precipitates, which present similar hardness to that of YG6 (Table 3), the penetration of YG6 asperities into the HEAs was sensibly resisted. This can markedly reduce the plowing force (friction force), Furthermore, the structure that the soft FCC solid solution surrounding the hard phase can enable the hard phase to move relatively freely, it could make the hard phase move downward to some extent, when subject to heavy stress, this could reduce the probability of the micro-fracture. However, these precipitates also experience some mechanical damages, mainly due to the low toughness. They will fracture. When the interfacial bonding is weak, the precipitate will also be pull-out by the shear stress (asperity f). these explain the continuous reduction of friction coefficient as well as the wear caused by micro-cutting with the Mo element. However, when the Mo molar ratio is too high, such as the volume fraction of 77.5% in Mo1.5, the contacting surface is almost entirely covered by these brittle intermetallic, as shown in Figure 13e. it changes into a significant hard phase-hard phase interaction. This makes the hard and brittle secondary phase suffer from micro-fracture easily, resulting in a higher friction coefficient and material removal rate. Furthermore, the precipitate also works as hard obstacles to resist the plow by the hard asperities or abrasive particles in the sliding, attributing to the superior hardness of 17 GPa. It could substantially reduce the abrasive wear, especially micro-cutting, which is the dominant wear mechanism for Mo0, Mo0.3, and Mo0. 5. Such claims are consistent with the results obtained by Deng et al. [19], who reveals that Mo0-0.3 exhibited the same wear mechanisms.

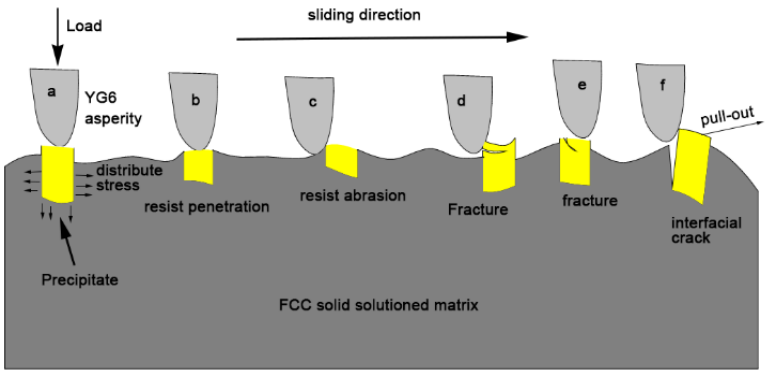


Figure 14. The schematic diagram of the behavior of precipitates in the wear process.

The analysis of the cross-sections reveals that the size of the hard precipitate also plays a key role in the wear resistance. As shown in Figure 11f that the width of the plowing groove is about 20 μm, if the diameter of the precipitate is smaller than 20 μm, the precipitate will be plowed away along with the ductile FCC solid solution, as shown in Figure 13c. Therefore, the diameter of the secondary phase shall be larger than 20 μm to resist the severe abrasion of the counter YG6 asperities, which is achieved for Mo1 HEA. This study explores the effect of Mo element in FeCoCrNiMo*x* high-entropy alloys in the mechanical properties and tribological behavior. It had provided some insights into the tribological behaviors of the HEAs, which are applied in mechanical elements subjecting

to relative motion. It will give the designers some enlightenment in the adjustment of chemical composition and microstructure of HEAs to achieve the best wear resistance.

5. Conclusions

The FeCoCrNiMox (x = 0, 0.3, 0.5, 1, 1.5 in molar ratio) high entropy alloys were fabricated by vacuum arc melting, and their microstructure, chemical composition, and mechanical properties were characterized. The friction and wear properties of the prepared alloys with the variation of Mo molar ratio were evaluated. We have explored the differences in performance under different phase structures by regulating the changes in molybdenum content, and have discovered FeCoCrNiMo1 alloy with excellent comprehensive performance in application value. Some conclusions can be obtained as follows:

(1) The as-cast FeCoCrNiMo0 alloy has a simple FCC solid solutioned structure. The volume fraction of precipitates increases continuously with the Mo content, and the maximum value reaches 77.8% for FeCoCrNiMo1.5.

(2) The hardness of the FCC solid solution is strengthened when the Mo molar ratio increases from 0 to 0.3, further increase of the Mo element results in little change of the FCC solid solution hardness. However, the global hardness and yield stress of FeCoCrNiMox increases with the Mo element continuously due to the increased precipitation of the hard intermetallic. But the ductility deteriorates, and the FeCoCrNiMo1.5 HEA does not exhibit any plastic deformation before compressive fracture.

(3) The FeCoCrNiMo1 alloy shows the lower average friction coefficient and wear rate among the tested HEAs, due to the balanced achievement of strength and ductility. When the Mo molar ratio is less than 1, severe micro-cutting and delamination wear was the dominant wear mechanism. It changes to mild micro-cut with some micro-fatigue wear for FeCoCrNiMo1, and transits to severe micro-cut and micro-fatigue wear for FeCoCrNiMo1.5.

(4) When the Mo molar ratio is increased to 1.5, the overly high-volume fraction and brittle nature of μ precipitates are the causes for its higher wear rather than Mo1.

Author Contributions: Conceptualization, S.C. and Y.L.; methodology, Y.X.; formal analysis, S.C.; investigation, Y.X. and X.X.; writing—original draft preparation, Y.X.; writing—review and editing, Y.X., S.C.; and Y.L.; visualization, Y.Y.; supervision, Y.L.; project administration, X.W.; funding acquisition, W.L. All authors have read and agreed to the published version of the manuscript.

Funding: This research was funded by the Young Scientists Fund of the National Natural Science Foundation of China, grant number 51905213, the National Key R&D Program of China grant number 2017YFB0305100, the Science and Technology Planning Project of Guandong Province, China, grant number 2017B090003005, 2017A090905027, 2017B090903005, Natural Science Foundation of Guangdong, grant number 906055014066.

Institutional Review Board Statement: Not applicable.

Informed Consent Statement: Not applicable.

Data Availability Statement: Not available.

Conflicts of Interest: The authors declare no conflict of interest.

Abbreviations

HEAs	High entropy alloys
FCC	Face centered cubic
XRD	X-ray diffraction
SEM	Scanning electron microscope
EDS	Energy diffraction spectrum
TCP	topologically close-packed phases

References

1. Yeh, J.W.; Chen, S.K.; Lin, S.J.; Gan, J.Y.; Chin, T.S.; Shun, T.T.; Tsau, C.H.; Chang, S.Y. Nanostructured High-Entropy Alloys with Multiple Principal Elements: Novel Alloy Design Concepts and Outcomes. *Adv. Eng. Mater.* **2004**, *6*, 299–303. [CrossRef]
2. Cantor, B.; Chang, I.T.H.; Knight, P.; Vincent, A.J.B. Microstructural development in equiatomic multicomponent alloys. *Mater. Sci. Eng. A* **2004**, *375–377*, 213–218. [CrossRef]
3. Tong, C.J.; Chen, M.R.; Yeh, J.W.; Lin, S.J.; Chen, S.K.; Shun, T.T.; Chang, S.Y. Mechanical performance of the AlxCoCrCuFeNi high-entropy alloy system with multi-principal elements. *Metall. Mater. Trans. A* **2005**, *36*, 1263–1271. [CrossRef]
4. Sun, S.J.; Tian, Y.Z.; Lin, H.R.; Lu, S.; Yang, H.J.; Zhang, Z.F. Modulating the prestrain history to optimize strength and ductility in CoCrFeMnNi high-entropy alloy. *Scr. Mater.* **2019**, *163*, 111–115. [CrossRef]
5. Sun, S.J.; Tian, Y.Z.; Lin, H.R.; Yang, H.J.; Dong, X.G.; Wang, Y.H.; Zhang, Z.F. Achieving high ductility in the 1.7 GPa grade CoCrFeMnNi high-entropy alloy at 77 K. *Mater. Sci. Eng. A* **2019**, *740–741*, 336–341. [CrossRef]
6. Chuang, M.H.; Tsai, M.H.; Wang, W.R.; Lin, S.J.; Yeh, J.W. Microstructure and wear behavior of AlxCo1.5CrFeNi1.5Tiy high-entropy alloys. *Acta Mater.* **2011**, *59*, 6308–6317. [CrossRef]
7. Dai, C.D.; Zhao, T.L.; Du, C.W.; Liu, Z.Y.; Zhang, D.W. Effect of molybdenum content on the microstructure and corrosion behavior of FeCoCrNiMox high-entropy alloys. *J. Mater. Sci. Technol.* **2020**, *46*, 64–73. [CrossRef]
8. Ding, Q.; Zhang, Y.; Chen, X.; Fu, X.; Chen, D.; Chen, S.; Gu, L.; Wei, F.; Bei, H.; Gao, Y.; et al. Tuning element distribution, structure and properties by composition in high-entropy alloys. *Nature* **2019**, *574*, 223–227. [CrossRef] [PubMed]
9. Wu, Z.; Bei, H.; Pharr, G.M.; George, E.P. Temperature dependence of the mechanical properties of equiatomic solid solution alloys with face-centered cubic crystal structures. *Acta Mater.* **2014**, *81*, 428–441. [CrossRef]
10. Gludovatz, B.; Hohenwarter, A.; Catoor, D.; Chang, E.H.; George, E.P.; Ritchie, R.O. A fracture-resistant high-entropy alloy for cryogenic applications. *Science* **2014**, *345*, 1153–1158. [CrossRef] [PubMed]
11. Liu, W.H.; Lu, Z.P.; He, J.Y.; Luan, J.H.; Wang, Z.J.; Liu, B.; Liu, Y.; Chen, M.W.; Liu, C.T. Ductile CoCrFeNiMox high entropy alloys strengthened by hard intermetallic phases. *Acta Mater.* **2016**, *116*, 332–342. [CrossRef]
12. Zhu, J.M.; Fu, H.M.; Zhang, H.F.; Wang, A.M.; Li, H.; Hu, Z.Q. Microstructures and compressive properties of multicomponent AlCoCrFeNiMox alloys. *Mater. Sci. Eng. A* **2010**, *527*, 6975–6979. [CrossRef]
13. Miao, J.; Guo, T.; Ren, J.; Zhang, A.; Su, B.; Meng, J. Optimization of mechanical and tribological properties of FCC CrCoNi multi-principal element alloy with Mo addition. *Vacuum* **2018**, *149*, 324–330. [CrossRef]
14. Shun, T.T.; Chang, L.Y.; Shiu, M.H. Microstructure and mechanical properties of multiprincipal component CoCrFeNiMox alloys. *Mater. Charact.* **2012**, *70*, 63–67. [CrossRef]
15. Lyu, Z.; Lee, C.; Wang, S.Y.; Fan, X.; Yeh, J.W.; Liaw, P.K. Effects of constituent elements and fabrication methods on mechanical behavior of high-entropy alloys: A review. *Metall. Mater. Trans. A* **2019**, *50*, 1–28. [CrossRef]
16. Li, W.P.; Wang, X.G.; Liu, B.; Fang, Q.H.; Jiang, C. Fracture mechanisms of a Mo alloyed CoCrFeNi high entropy alloy: In-situ SEM investigation. *Mater. Sci. Eng. A* **2018**, *723*, 79–88. [CrossRef]
17. Niu, Z.Z.; Wang, Y.Z.; Geng, C.; Xu, J.; Wang, Y. Microstructural evolution, mechanical and corrosion behaviors of as-annealed CoCrFeNiMox (x = 0, 0.2, 0.5, 0.8, 1) high entropy alloys. *J. Alloys Compd.* **2020**, *820*, 153273. [CrossRef]
18. Bae, J.W.; Park, J.M.; Moon, J.; Choi, W.M.; Lee, B.J.; Kim, H.S. Effect of μ-precipitates on the microstructure and mechanical properties of non-equiatomic CoCrFeNiMo medium-entropy alloys. *J. Alloys Compd.* **2019**, *781*, 75–83. [CrossRef]
19. Deng, G.; Tieu, A.K.; Su, L.; Wang, P.; Wang, L.; Lan, X.; Cui, S.; Zhu, H. Investigation into reciprocating dry sliding friction and wear properties of bulk CoCrFeNiMo high entropy alloys fabricated by spark plasma sintering and subsequent cold rolling processes: Role of Mo element concentration. *Wear* **2020**, *460–461*, 203440. [CrossRef]
20. Shun, T.T.; Hung, C.H.; Lee, C.F. The effects of secondary elemental Mo or Ti addition in Al0.3CoCrFeNi high-entropy alloy on age hardening at 700°C. *J. Alloys Compd.* **2010**, *495*, 55–58. [CrossRef]
21. Gengxiang, H.; Xun, C.; Yonghua, R. *Fundamentals of Materials Science*; Shanghai Jiao Tong University Press: Shanghai, China, 2000.
22. Archard, J.; Hirst, W. The wear of metals under unlubricated conditions. *Math. Phys. Sci.* **1956**, *236*, 397–410.
23. Deng, G.; Tieu, A.K.; Lan, X.; Su, L.; Wang, L.; Zhu, Q.; Zhu, H. Effects of normal load and velocity on the dry sliding tribological behaviour of CoCrFeNiMo0.2 high entropy alloy. *Tribol. Int.* **2020**, *144*, 106116. [CrossRef]
24. Wen, S.; Huang, P. *Tribology Principle*; Tsinghua University Press: Beijing, China, 2002.
25. Suh, P.N. The delamination theory of wear. *Wear* **1973**, *25*, 111–124. [CrossRef]
26. Stachowiak, G.; Batchelor, A.W. *Engineering Tribology*; Butterworth-Heinemann: Oxford, UK, 2013.
27. Pauschitz, A.; Roy, M.; Franek, F. Mechanisms of sliding wear of metals and alloys at elevated temperatures. *Tribol. Int.* **2008**, *41*, 584–602. [CrossRef]
28. Huttunen-Saarivirta, E.; Kilpi, L.; Hakala, T.J.; Metsäjoki, J.; Ronkainen, H. Insights into the behaviour of tool steel-aluminium alloy tribopair at different temperatures. *Tribol. Int.* **2018**, *119*, 567–584. [CrossRef]
29. Gengxiang, H.; Xun, C.; Yonghua, R. *Fundamentals of Materials Science*, 2nd ed.; Shanghai Jiaotong University Press: Shanghai, China, 2006.
30. Zheng, B.; Li, W.; Tu, X.; Song, S.; Huang, W. Effect of ZTA ceramic particles strengthened high chromium white cast iron on three-body abrasion behavior. *Mater. Res. Exp.* **2019**, *6*, 116581. [CrossRef]
31. Holz, D.; Janssen, R.; Friedrich, K.; Claussen, N. Abrasive wear of ceramic-matrix composites. *J. Eur. Ceram. Soc.* **1989**, *5*, 229–232. [CrossRef]

32. Tabor, D. The physical meaning of indentation and scratch hardness. *Br. J. Appl. Phys.* **1956**, *7*, 159–166. [CrossRef]
33. Bowden, F.P.; Moore, A.J.W.; Tabor, D. The Ploughing and Adhesion of Sliding Metals. *J. Appl. Phys.* **1943**, *14*, 80–91. [CrossRef]